

Solar powered UAV with remote monitoring and thermal imaging system for transmission line inspection

Maarten Van Jaarsveld¹, Brandon Du Toit¹, Immanuel N. Jiya^{1*}, Rupert Gouws¹

¹ School of Electrical, Electronic and Computer Engineering North-West University, Potchefstroom 2520, South Africa

*Corresponding author E-mail: immanueljiya@ieee.org

Abstract

Eskom, South Africa's electricity utility organisation, dedicates an enormous amount of resources in the form of time and money to visually inspect the conditions of these transmission lines on an annual basis. These transmission lines are inspected normally by means of a foot patrol or by flying a helicopter in close proximity to the line. During the foot patrol inspection, a team of people walk from pylon to pylon and inspect the transmission line. Binoculars and IR or corona detection cameras are typically used to aid their inspection. The transmission lines are often located in geographical areas where it is difficult to access these lines by foot; it then becomes necessary to use a helicopter to inspect the line. Various hazards exist in operating a helicopter in such close proximity to these transmission lines and the process of hiring or employing trained specialists to operate the helicopter and the accompanying equipment is costly. Inspecting transmission lines by means of foot patrols or by helicopter is not only costly, but dangerous as well. This paper proposes a new method of transmission line inspection using a solar powered UAV with the inspection equipment mounted on it. The addition of the solar cells to the UAV was beneficial to the overall flight performance of the aircraft, only contributing 6% to the aircrafts total weight, while supplying 20% to 35% of the aircrafts energy needs. This resulted in an approximate increase in the flight range of the aircraft by about 20%.

Keywords: Solar power; UAV; Transmission Line Inspection; Remote Monitoring.

1. Introduction

The growing population and industrialization in Africa and other countries of the world come with huge needs for electrical energy. Unfortunately, electricity is not usually used where it has been generated, there is need to transfer this energy from where it has been generated to consumers. This is often done using transmission lines. The maintenance of these transmission lines is pivotal to effective delivery of energy to consumers. Transmission line inspection is a pivotal maintenance scheme for these assets to perform optimally.

Over the years, manual transmission line inspection has been implemented to detect fault points and hotspots on the transmission line. In this system of monitoring inspection personnel travels through the path of the transmission line with the inspection equipment to conduct the inspection, but this can be a very tedious and difficult task because of the difference in terrain and other dangerous environmental hazards.

Eskom is a South African electricity public utility that generates approximately 95% of the electricity used in South Africa [1]. Transmission lines are an essential component of the national electrical utility grid, used to carry generated electricity from the point of the generation to electrical substations and consumers.

Eskom maintains the transmission network that transports the high voltage electricity between generation facilities and distribution centres. This transmission network consists of 377,287 km of power lines that needs to be maintained as well as monitored so that preventive maintenance can be done [2].

Eskom dedicates an enormous amount of resources in the form of time and money to visually inspect the conditions of these transmission lines on an annual basis. These transmission lines are

inspected normally by means of a foot patrol or by flying a helicopter in close proximity to the line. During the foot patrol inspection, a team of people walk from pylon to pylon and inspect the transmission line. Binoculars and IR or corona detection cameras are typically used to aid their inspection. The transmission lines are often located in geographical areas where it is difficult to access these lines by foot; it then becomes necessary to use a helicopter to inspect the line.

Various hazards exist in operating a helicopter in such close proximity to these transmission lines and the process of hiring or employing trained specialists to operate the helicopter and the accompanying equipment is costly. Inspecting transmission lines by means of foot patrols or by helicopter is not only costly, it is reported that these routine helicopter inspections cost around \$1,200 per hour, but dangerous as well [3]. Developing a system that will firstly reduce the operating cost of inspections and reduces the safety risks involved would be beneficial to Eskom.

The transmission line network (National Grid) in South Africa is maintained and inspected by Eskom. The inspection of these transmission lines are primarily done by implementing patrols on foot next to the transmission lines or by using a helicopter to observe the lines. Both of these inspection techniques are time consuming and costly processes that pose a safety risk to the people performing the inspections [4], [5]. A system/method needs to be developed that will allow Eskom to be able to monitor the transmission lines in an efficient, cost-effective and safe manner.

The power industry has been increasingly interested in the use of UAV technology as a tool to inspect transmission lines [5], [6]. An inspection team transports a UAV to the inspection site, were the UAV is then flown, taking high-definition images/videos of the transmission line. These UAV's provide a higher level of detail of the transmission lines to the inspection team, compared to

the inspection team using binoculars and cameras to inspect the lines from a var. UAV's have become more affordable for civilian and industrial applications, owing to the advancements and interests in UAV technology.

A variety of UAV platforms are used in the power industry to inspect the power lines [7], [8]. These platforms typically make use of multirotor aircrafts or helicopters. A multi-rotor aircraft and a helicopter used in the power line inspection industry are shown in figure 1 and 2 respectively. These platforms are excellent at observing the power lines from close proximity, but are limited by a relative short operational time. They can only be used to inspect a short distance of line without recharging/replacing their energy source.

Power line inspection robots have been developed by a few organisations [9], [10]. These robots are placed on the power lines, were they then crawl along the length of line, while capturing information about the power line. These robots are equipped with cameras and thermo-infrared imagers which provide detailed information on the condition of the transmission line [9]. Some of these robots are also capable of completing basic repair work on the transmission lines.

These power line inspection robots move slowly along the lines and elaborate techniques have to be used to ensure these robots are able to traverse the support structures and equipment. These robots are heavy and can only inspect a relatively short distance of line from their controlling base station, limiting their practical usage.

These alternative systems allow Eskom to monitor the National Grid in a more cost-effective and safe manner. These systems are capable of obtaining information from the transmission lines with great detail, but these systems do have shortcomings. These systems: 1) have a short operating time, 2) are limited by the transmission line tower structure, 3) and ultimately can only inspect a short length of transmission line within a reasonable amount of time.

The primary objective of this research was to develop a system that will be able to transport a monitoring system, which is also presented in this paper, over a long distance. The system made use of solar cells to extend the usable range of the system.

2. Design and component selection

A preliminary conceptual design of the proposed solution is shown in figure 5. An existing fixed wing UAV or RC aircraft will be used in this project, seeing that the goal of project is not to design a fixed wing aircraft. The aircraft will be retrofitted with solar cells that will provide the aircraft with additional energy during flight.

A charge controller will be designed that will charge the batteries on-board the aircraft. A power monitoring system will also be designed that will be used to determine the estimated flight range of the aircraft, ensuring that the aircraft will be able to return to the point of take-off. This will be done by monitoring the power consumption of the motor and the monitoring system, as well as the energy available from the solar cells and the batteries. The power monitoring system will also obtain information such as the altitude and airspeed of the aircraft from the flight controller. Using the obtained information the system will be able to calculate an estimated flight range of the aircraft.

The user will plan a route for the aircraft by creating GPS waypoints. The transmission line inspection system on-board the aircraft will obtain the necessary information from the transmission lines as it flies through these waypoints. This information will then be available to the user for analysis.

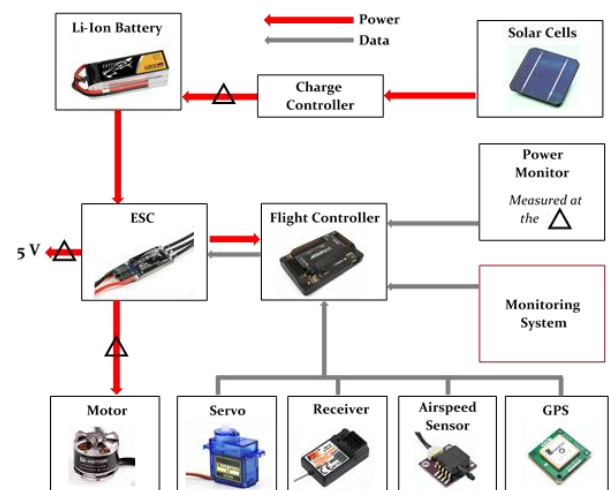


Fig. 1: Concept Design.

2.1. Airframe and flight controller

The X-UAV Talon was identified as the best option for this project. The Skywalker X8 would also be a good option for the project, but the Skywalker was not locally available in South Africa, while the Talon is.

A powered monoplane identified from the RC industry that was suitable for the project was the X-UAV Talon. This aircraft is modelled after the Lockheed Martin Desert Hawk that was used by the United States Army [11]. The aircraft has a relatively large wing area as well as a large wingspan. It is also possible to lengthen the wings of the aircraft, increasing the wing area of the aircraft as well as the flight stability. The aircraft also has a relatively large cargo bay, which is required for this project to contain the monitoring system.

The Pixhawk flight controller was identified as the best solution for this project due to its accuracy, relatively easy implementation and the user interface that is available for this controller.

Pixhawk is an open-hardware project that provides an autopilot hardware solution to be used for autonomous flight systems. The Pixhawk flight controller can use other open-source software flight controller firmware, such as the firmware developed by APM, described above. This flight controller has more advanced sensors, a faster CPU clock frequency and more communication interfaces when compared to the APM 2.6. The Pixhawk is more expensive when compared with the APM 2.6, but the systems sensor array and processor is more advanced.

The Pixhawk can also be configured and programmed from the Mission Planner software created by ArduPilot.

2.2. Power system

Two major systems needed to be designed for this research with regards to the Power system of the aircraft and they are:

- i) Charge Controller
- ii) Power Monitoring System.

2.2.1. Charge controller

The design specifications of the charge controller will be determined by the output voltage of the solar panels as well the power that these panels will output in optimum conditions. The expected output power of the panels was determined by the amount of panels that will fit on the aircraft.

SolidWorks® was used to determine the amount of panels that would fit on the aircraft. Figure 2 shows a Stereo Lithography scan of the aircraft from the supplier, while Sunpower's Maxeon C60 solar cells were drawn in SolidWorks®. The aircraft is shown in red, to contrast the solar cells with the background.

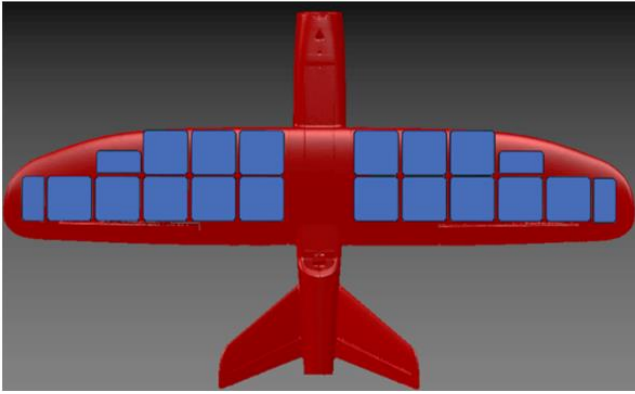


Fig. 2: Solar Cell Placement.

Sunpower states that their solar cells produce 3.3 W of power per cell. From figure 2 it is approximated that 18 cells can be placed on the aircraft. If all of these cells operate at maximum efficiency and without any loss, a total of 59.4 W of power will be generated. The solar cells on each wing were connected in series to a charge controller. These cells produce a nominal voltage of 0.5 V, each solar array will then produce a voltage of about 5 V in ideal conditions.

The solar array on each wing has its own MPP charge controller, so that in the case of the failure of one of the controllers, or that one of the solar cells fails, half of the power from the solar cells is still available. A MPP charge controller was designed to be able to charge a 4 cell Li-PO battery at 40 W.

The specifications for the MPP charge controller are as the follows:

- Capable of boosting the voltage of the solar array from about 5 V to 14.4 V (14.4 V is the nominal voltage of a 4 cell Li-PO battery).
- Perform maximum power point tracking.
- Deliver 40W of power to battery.

The block diagram of the implementation of the MPP charge controller is shown in figure 3. The current and voltage of the solar array will be measured, to be able to determine the power developed by the panel. A boost converter will be used to convert the voltage from the solar array to the voltage of the batteries.

A microcontroller, such as those produced by Atmel, was used to monitor the power produced by the solar array. A MPP algorithm was used to operate the solar array at its MPP. The microcontroller then modified the duty cycle of the boost converter to operate the solar array at its MPP.

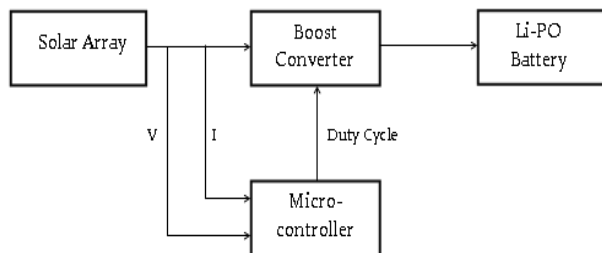


Fig. 3: Block Diagram of MPPT Charge Controller.

The design of the MPP charge controller was further divided into two sections,

- The design of the boost converter,
- The algorithm to be used by the microcontroller.

2.2.1.1. Design of the boost converter

For a boost converter the essential component values that need to be determined are the values of the inductor, capacitor and the maximum ratings of the switching device and diode. Figure 4 shows the voltage and current waveforms through these devices as the switching device (q) switches.

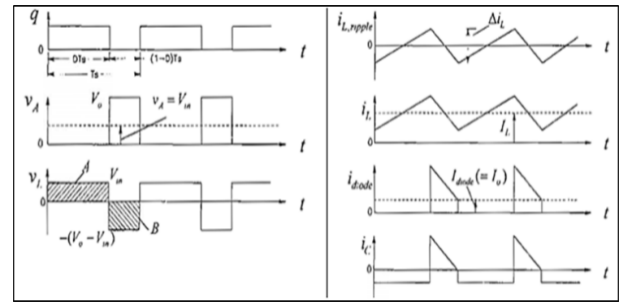


Fig. 4: Boost Converter Waveform [12].

The converter has the following specifications: $V_{in} = 2 \text{ V to } 5 \text{ V}$, $V_{out} = 14.4 \text{ V}$, $F_s = 62.5 \text{ kHz}$, $P_{out} = 40 \text{ W}$, $P_{out-min} = 5 \text{ W}$.

The ratio of the output voltage to the input voltage is

$$\frac{V_{out}}{V_{in}} = \frac{1}{1-D} \quad (4)$$

The voltage over an inductor is equal to the inductance of the inductor times the rate of change of current through the inductor. In mathematical form,

$$V_L = L \frac{di}{dt} \quad (5)$$

Taking the voltage over the inductor when the switching device is closed, as shown in figure 4, is:

$$V_{in} = L \frac{\Delta I}{DT_s} \quad (6)$$

Where D is the duty cycle of the switching device and T_s is the period of the switching signal. Similarly when the switching device is open,

$$V_{out} - V_{in} = L \frac{\Delta I}{(1-D)T_s} \quad (7)$$

The maximum and minimum duty cycles are calculated if the input voltage ranges from 2 V to 5 V.

For $V_{in} = 2 \text{ V}$, $D = 0.86$, and $V_{in} = 5 \text{ V}$, $D = 0.65$.

The duty cycle will thus range from approximately 0.65 to 0.86.

The boost converter will be operated in continuous conduction mode. Observing the current waveform of the current flowing through the diode in figure 4 we note that the current is equal to the current flowing through the inductor when the switching device is turned off. To ensure that the boost converter operates in CCM, the change in the current should at least be equal to

$$\Delta I = \frac{2I_{out-min}}{1-D} \quad (8)$$

Combining equation (4) and (7), and substituting ΔI with equation (8), the value for the inductor is given by the following equation,

$$L = \frac{D(1-D)^2 V_{out} T_s}{2I_{out-min}} \quad (9)$$

The minimum value for the inductor can then be found by differentiating $D(1-D)^2$. This results in a duty cycle of 0.33 that will result in the minimum value of the inductor for CCM. Seeing that the minimum duty cycle is 0.65, the minimum value of the inductor for CCM will occur at 0.65. Substituting 0.65 in equation (9) yields,

$$L = \frac{D(1-D)^2 V_{out} T_s}{2I_{out-min}} = \frac{0.65(1-0.65)^2 \times 14.4 \times 1.6 \times 10^{-5}}{2(0.347)} = 26.4 \mu\text{H}$$

The minimum value for the capacitor can be calculated by observing the current waveform through the capacitor in figure 28. The

current through a capacitor is equal to the capacitance of the capacitor times the rate of change of the voltage over the capacitor. In mathematical form,

$$I_C = C \frac{dV}{dt} \tag{10}$$

Noting that the output current of the boost converter is 2.77A, the required capacitance to produce a voltage ripple less than 2% from equation 10 is,

$$C = \frac{I_o \Delta T}{\Delta V} = \frac{I_o DT_s}{0.05 \times V_{out}} = 131 \mu F$$

The diode in the circuit was selected as a Schottky diode, seeing that this type of diode has a low forward voltage drop and is capable of fast switching. The average forward current that the diode can handle should be at least 4A. A MOSFET was used as the switching device in the boost converter. The MOSFET should have a voltage rating of two times the output voltage to include a safe operating margin. The MOSFET also should have a current rating of 8A. The capacitor as stated should have capacitance of 52 uF, as well as a voltage rating of at least 25V, a low ESR and good high frequency characteristics.

The requirements for the MOSFET, diode, capacitor and inductor are given in table 1.

Table 1: Designed Component Values

	Inductor	Capacitor	Diode	MOSFET
Minimum Average Current (A)	8		4	8
Minimum Voltage (V)		25	25	25
Designed Value	26.4 uH	131 uF		

The design of the boost converter was verified and tested in LtSpice. The Spice models of the diode and MOSFET were used in the simulation, to increase the accuracy of the simulations predictions. Using a pulse width amplitude modulated input signal to the gate of the MOSFET, at a duty cycle of 65%, the theoretical calculations estimated that the boost converter will output 14.4V. From the simulations we find the voltage to be 13.85V.

The diode used in the circuit has a forward voltage drop of 0.5V which the theoretical calculations didn't take into account. This accounts for the difference in the simulated output voltage and the theoretical output voltage. The voltage ripple on the output of the simulated circuit is also within satisfactory limits. A voltage ripple of 120mV is estimated by the simulation, when a 200 uF capacitor was used.

The boost converter performed as expected in the simulation. The ratio of the output voltage to the input voltage is as expected, if the forward voltage drop of the diode is taken into account. An inductor with a value twice as large as was calculated was used, as to prevent any circumstance in which the inductor reaches saturation.

2.2.1.2. MPPT controller implementation (algorithm to be used by the microcontroller)

In order to operate the solar panels at their MPP, a MPP tracking algorithm needs to be employed on some controller. The tracking algorithm monitors the current and voltage of the panel, to determine the power produced by it. The controller then varies the load on the panel by varying the duty cycle of the switching device in the boost converter.

The Perturb and Observe algorithm was used by the controller to operate the panel at its MPP. This algorithm is a type of hill climbing method, in which the voltage of the panel is increased and the response of the panel is observed. If the power output of the panel increased, the controller will continue to increase the voltage of the panel. If the power output decreased, the controller will decrease the voltage of the panel. This algorithm oscillates the power output of the panel around the MPP of the panel. The program flow implemented in the controller is shown in figure 5.

From the flow diagram in figure 5 we observe that only two values need to be measured, while only one control output is needed. A microcontroller was used to implement the P&O algorithm in the charge controller. Seeing that the microcontroller only has to measure two values and be able to output one PWM signal, Atmel's Attiny 85 was used. This microcontroller has two PWM outputs, three analogue inputs and is available in a DIP 8 package, making it quite compact. The microcontroller was powered from the 5V supply from the BEC of the ESC.

To measure the current flowing from the solar panel, a shunt resistor was used. A shunt resistor is a resistor, normally with a low resistance, used to approximate the current flowing through it by measuring the voltage drop over the resistor. Ohm's law is then used to determine the current. Using a low resistance resistor ensures that the power loss via the resistor is minimal and that it does not affect the rest of the circuit notably. The only problem with using a shunt resistor is that the voltage drop over the resistor can be too small to provide an adequate resolution. The INA210 IC from Texas Instruments was used to amplify the voltage drop over the shunt resistor. This IC then amplifies the measured voltage drop by 200, to provide an adequate measurement resolution for the microcontroller.

To verify the MPP algorithm shown in figure 5, the MPP system was implemented and simulated in Matlab's Simulink. A model for a solar panel was obtained from a MathWorks® toolbox. A boost converter was implemented in Simulink to step up the solar panels supplied voltage. The stepped up voltage is then applied across a resistive load. A custom function block, called MPPT, was used to control the duty cycle applied to the boost converter. The MPP algorithm shown in figure 5 was implemented in this custom function block to control the duty cycle.

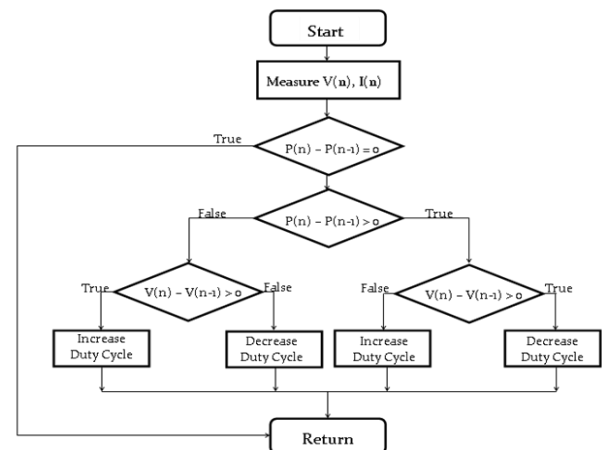


Fig. 5: MPPT Algorithm.

The goal of this simulation was to verify that the MPPT algorithm works correctly and would perform as expected. The MPPT function block shown in figure 6 obtains the current and voltage generated by the solar panel. This block then outputs the required duty cycle to the boost converter. The power generated by the solar panel was also passed through a smoothing filter to graph the power generated by the solar panel and the boost converter. The functional block of the MPPT block is shown in figure 7. The boost converter block implements a typical boost converter design and also measures the power output of the boost converter, so that the power output of the boost converter can be compared with that of the solar panels output power. To be able to verify the operation of the MPPT algorithm, the solar panel was radiated by different levels of light intensity. We would thus expect that for different amounts of light intensity that the controller would adjust the duty cycle applied to the boost converter. To verify that the algorithm works correctly, different light intensities were applied to the solar panel, while the output power of the boost converter and the output of the solar panel were monitored.

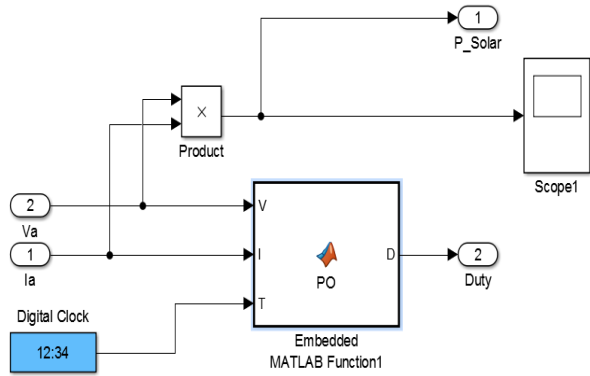


Fig. 6: MPPT Functional Block.

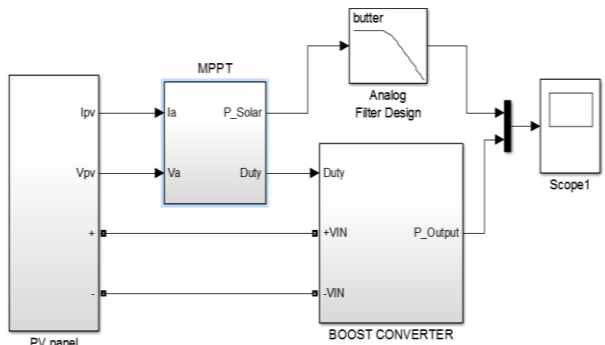


Fig. 7: MPPT System Implemented In Simulink.

The duty cycle applied to the boost converter by the MPPT controller at steady-state was 62%. For other values of light intensity, the output power of the boost converter should still follow the power of the solar panel, but should apply a different duty cycle seeing that the maximum power point (MPP) changes with the applied light intensity.

The duty cycle applied by the MPPT controller at steady-state was 47% when a medium level of light radiation was applied to the solar panel. The MPPT controller thus adjusted the duty cycle applied to the boost converter to operate the solar panel at its MPP.

2.2.2. Power monitoring system

The power monitoring system monitors the power consumption of the brushless motor and the monitoring system, while the power developed by the solar panels is also monitored. The power monitor system is used to determine the estimated range of the aircraft. By obtaining the altitude and airspeed of the aircraft from the flight controller, the system calculates the estimated range of the aircraft.

To monitor the total power consumption and the power available from the solar cells, the power consumption and the following points in the system was measured:

- Energy consumption of the motor.
- The energy flowing to the flight controller, monitoring system, charge controller and the power monitoring system.
- The energy flowing from the charge controller to the battery.

The energy flowing through each of these points that are monitored varies and is different for each of the measuring points. A power measuring IC was used to measure the power consumption by multiplying the current measured using a shunt resistor and the voltage at the point of measurement. Three of these power measuring IC's were used to measure the instantaneous power at each measuring point. The INA 219 IC from Texas Instruments was used. This IC outputs the power measured via I2C. This is specifically useful for this project, seeing that the monitoring system, developed by Brandon du Toit, uses a Raspberry Pi to control the monitoring system. The power measurements are sent via I2C to the Raspberry Pi, where the average power consumption is calculated. The Raspberry Pi also uses the information obtained from

the flight controller to calculate the estimated flight range of the aircraft.

The Raspberry Pi is used to calculate the estimated flight range of the aircraft as it eliminates the need for an additional microcontroller to be used to do this estimation. Each power measuring IC has its own I2C address. This allows the microcontroller to obtain the power usage from each measuring point. The method used to calculate the estimated flight range of the aircraft is given in figure 8.

The INA 219 chip amplifies the voltage drop over the shunt resistor to calculate the current flowing through the shunt resistor using Ohm's law. The chip has multiple current sensing voltage ranges, from 40mV to 320mV. The 40mV voltage range scale was used, as to allow a resistor with a smaller resistance to be used. This minimizes the power dissipated in the shunt resistor. Table 2 contains the expected current that was to be measured, the value of the shunt resistor, the voltage deflection and the power loss in the shunt resistor, as was used in the design of the power monitor.

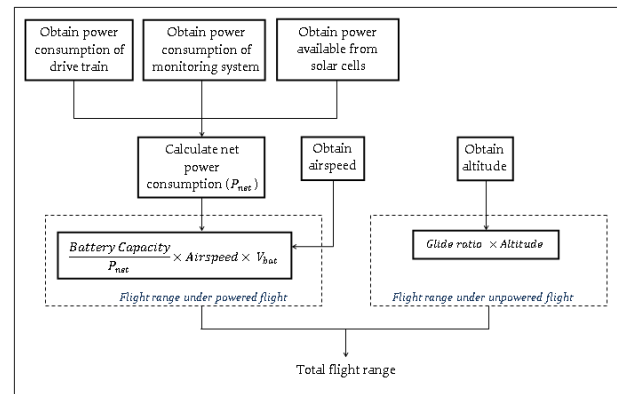


Figure 8: Flight Range Estimation.

Table 2: Power Monitoring System Component Specifications

Measuring Point	Expected Maximum Current (A)	Shunt Resistor (mΩ)	Voltage Drop (mV)	Power Loss
Drive Train	50	0.75	37.5	1.875 W
Monitoring System	2	15	30	60 mW
Solar Cells	5	8	40	200 mW

2.3. Propulsion system

The manufacturer of the X-UAV Talon recommends that a brushless motor capable of providing at least 500W of power to the rotor shaft be used in the propulsion system.

A brushless motor was then selected to be used in this aircraft, due to the recommendations from the manufacturer. Two brushless motors from different manufacturers were used in previous projects at the university. Both of these motors are capable of supplying more than 500W of power to the rotor. These two motors are the Aerodrive SK3-4240 620kV and the Turnigy D3548/4 1100KV brushless motors. The kV rating of the motor refers to the revolutions per minute that the rotor of the motor will rotate at per voltage applied to the unloaded motor.

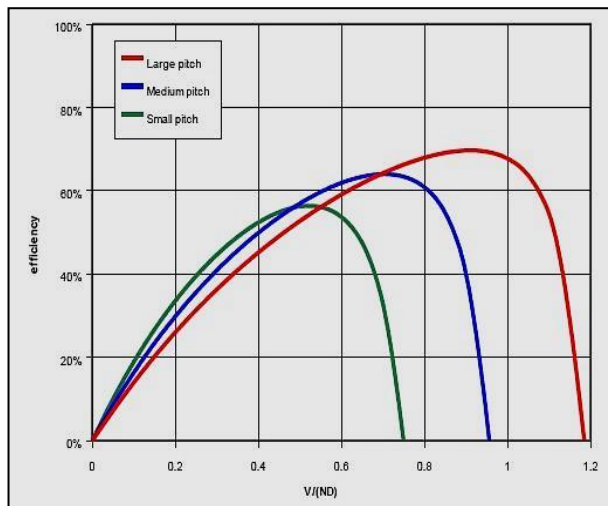


Fig. 9: Propeller Efficiency Per Advance Ratio [14]

The brushless motor with the lower kV rating will require a propeller with a larger pitch to produce the same amount of thrust than a brushless motor with a higher kV rating with a smaller pitch. The pitch of the propeller influences the maximum efficiency of a certain propeller. Figure 9 shows how the maximum efficiency of a propeller differs with pitch. Also note that the larger the pitch of the propeller, the maximum efficiency point will occur at a higher velocity than that of a smaller pitch propeller. A larger pitch propeller is more efficient than a smaller pitch propeller because the larger propeller needs to make fewer revolutions per the same advancement in the air. Fewer revolutions per unit time will reduce the loss in energy due to the drag of the propeller.

The motor with a lower kV using a propeller with a larger pitch when compared to that of a higher kV motor with a smaller pitch will be more efficient, if the electrical losses in the two motors are comparable. The Aerodrive SK3-4240 620kV motor with a propeller with a large pitch was thus used in this project.

The Aerodrive SK3-4240 620kV brushless motor was identified as the motor that would be used in the project due to it being available from previous projects and the probability of being more efficient than the Turnigy D3548/4 1100KV brushless motor. The manufacturer states that the brushless motor will draw a maximum of 48A with a 4 cell Li-Po battery. An ESC capable of delivering 60 A was chosen to provide power to the motor, while the ESC will only provide 80% of the maximum current it can provide if the motor is operating at full load. The ESC that was selected was available from previous projects. The ESC is the Turnigy Plush 60A ESC.

2.4. Monitoring system concept design

Taking a look at the hardware concept design in figure 10, the main components used in the design of the transmission line monitoring system will be an on-board single-board computer, some form of FLIR imaging camera, a photo/video camera, two wireless transceivers and some form of GUI to display the captured data for the user. The UAV will take off on a pre-planned mission defined by the user. It will fly to set waypoints and once at these waypoints, will begin capturing data. This data will include, but may not be limited to, FLIR images, colour images, UAV airspeed and GPS location. This data will be stored on the SBC's internal storage until the UAV returns to its "home base". Once there it will connect to a dedicated server, where it will then transfer the data to a host computer. On the host computer the data will be sorted and stored in a database from where it will be accessible to the user for viewing.

Figure 11 shows the envisioned program flow for the monitoring system. It begins by powering the SBC and external components, thereafter the SBC boots and begins initialization. When this process has completed and the UAV is airborne the SBC polls a cer-

tain GPIO pin that will be triggered by the flight computer when it is time to start capturing data. Upon being triggered the SBC captures the two types of images and requests the current GPS position along the airspeed. This data is saved onto the on-board SD card and the SBC continues polling for the next trigger. If at any time the operator wishes to know the UAV's status it can be requested via the long range transceiver. When the UAV has returned to base the captured data is uploaded to the server computer and the UAV is shut down.

Figure 12 shows the final planned design and layout for the web-based GUI. The interface displays both the normal-coloured image and FLIR thermal image side by side, with the option to enlarge. It shows, in text, the GPS location where the photos were taken, the altitude at which they were taken and the UAV's airspeed at the time. To the user there are options to flag the photo's with a check box if a problem is spotted and to add comments to specify what the problem is or a possible course of action. There are Next, Previous and Home buttons to move on, move back or return to the home screen respectively.

A MySQL database was used to store the data for each day's mission. A database called Eskom was created that contains all the tables of data. A table structure with 8 fields was created for each day wherein the data was stored.

The ID field serves as the table's primary key and identifies the name of the images to be displayed using a 32-bit integer data type. Both imagePath and irImagePath are varchar(100) types, which can store up to 100 characters. This field stores the path to both the normal-coloured and thermal image relative to the PHP document that has to display the image. The GPS field is a varchar(50) field that stores the GPS position of the place the image was taken. Altitude and Airspeed are both of type double to accommodate decimal values to be more precise. The comments field is a varchar(200) field intended for operator comments when inspecting the images and the Flagged field is a tinyint(1) field meant to be used as a binary field, either 1 or 0. This indicates to the operator that he or someone else has identified a possible issue on a specific image.

The final planned program flow for the on-board system is similar to figure 13, but differs in that the monitoring system will also be doing the power monitoring calculations and as such an extra function block has been added to handle the measurements and calculations.

3. Implementation and results

The aircraft uses various components and systems to operate and fly. These components include the brushless motor, servos, ESC, LiPO battery, flight controller, the RC receiver and the RC transmitter. These components are the bare minimum components needed to fly the aircraft. The power monitoring circuit and the MPPT charge controller were designed and implemented to firstly monitor the power consumption of the aircraft and then secondly to control the flow of energy from the solar cells to the battery.

The MPP charge controller was firstly developed on a prototype Veroboard®. The performance of the charge controller was tested on the prototype board. After verifying that the performance of the MPP charge controller was sufficient, it was decided that it was not necessary to print the designed PCB for the MPP charge controller.

As discussed in the design section, the Maxeon c60 solar cells were used. These cells are somewhat flexible and can conform to small curvatures in the aircraft's wing. Two solar arrays were created, each one for each wing of the aircraft. The solar cells in each array were connected in series, producing an open circuit voltage of ± 6.6 V and a short circuit current of about 5A. A total of 22 solar cells were integrated into the aircraft, with 11 solar cells on each wing. Figure 14 shows the completely assembled aircraft with the solar cells integrated into the wings of the aircraft.

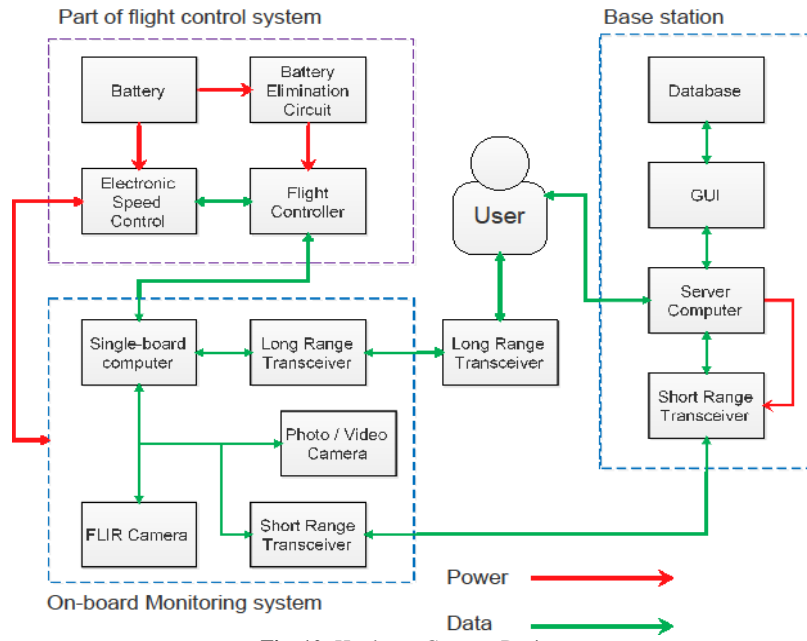


Fig. 10: Hardware Concept Design.

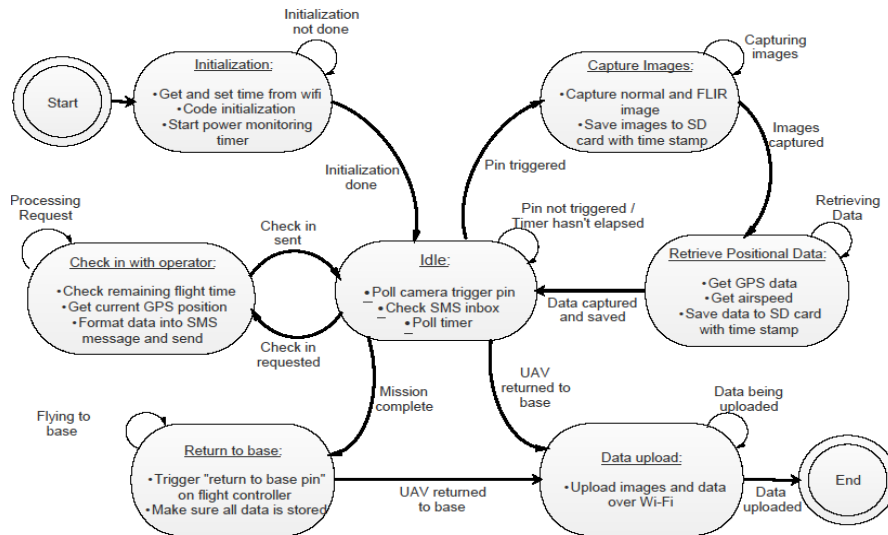


Fig. 11: Envisioned Program Flow.

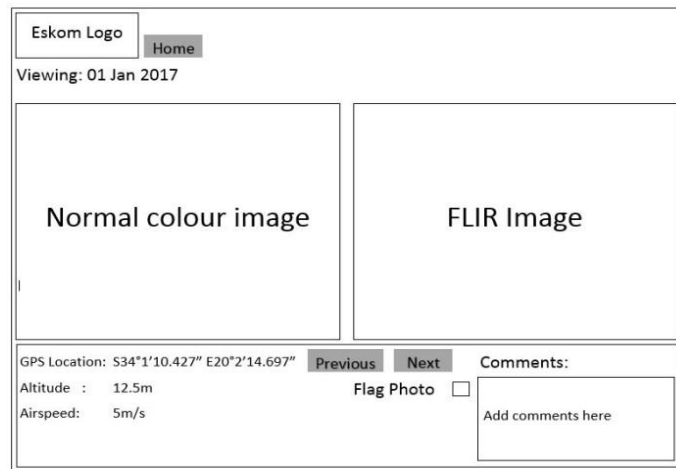


Fig. 12: Final GUI Design.

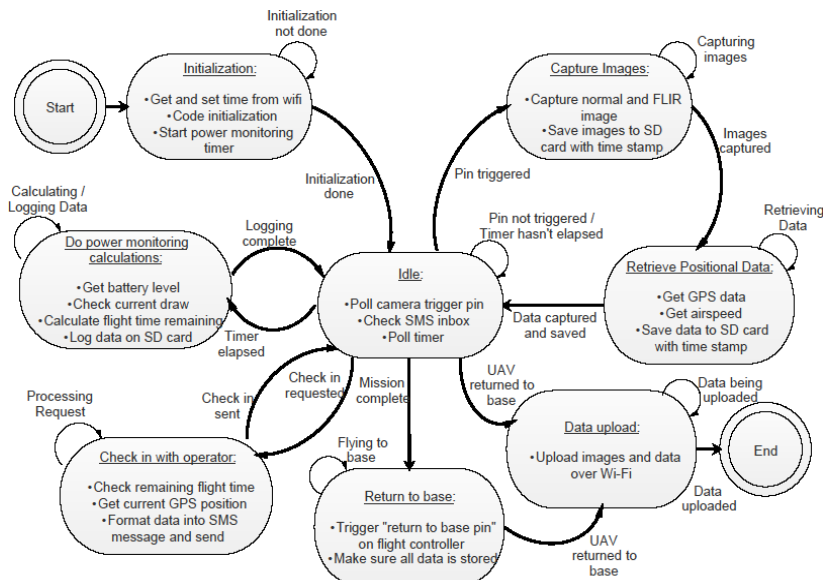


Fig. 13: Final Program Flow.



Fig. 14: Completed Aircraft with Integrated Solar Cells.

The solar cells were fixed to the wings of the aircraft by using d-c-fix®. Covering the solar cells with d-c-fix® did not negatively affect the performance of the solar cells and also increased the ruggedness of the aircrafts wings, but was somewhat difficult to apply to the aircraft without wrinkles and imperfections. The integrated aircraft, with all the designed system components are shown in figure 15. The components were placed in such a manner as to reduce the overall wiring needed to connect the various components. The annotations added to the figure shows which components were placed at the different locations in the aircraft. The batteries of the aircraft were placed as far forward as possible to ensure that center of gravity of the aircraft was as specified by the manufacturer of the aircraft.

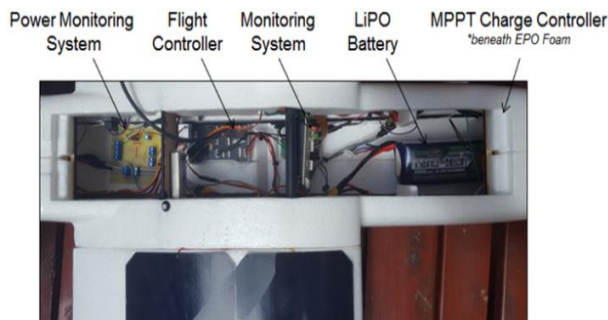


Fig. 15: Layout of Components within the Aircraft.

The operation of the power monitoring circuit was verified by measuring the current flowing to the device whose power had to be measured. The measured current was then compared against the current measured by the power monitoring circuit. The current was measured using a multimeter and then compared to the data that was transmitted to the computer. The data was transmitted

from the power monitoring circuit using I2C to an Arduino, which then transmitted the data to the computer. The same process was followed to verify the power consumption of the monitoring system.

To verify that the MPPT charge controller worked correctly and actually operated the solar panel at its MPP the following was done. A sweeping duty cycle was applied to the solar panels, to find the MPP of the solar panels for that irradiation level. The power output of the MPP charge controller operating under the Perturb & Observe algorithm was then measured while the solar panels were exposed to the same levels of irradiation. The results of this process is shown in figure 16, in which we note that the MPPT charge controller was operating the solar cells close to their maximum power point.

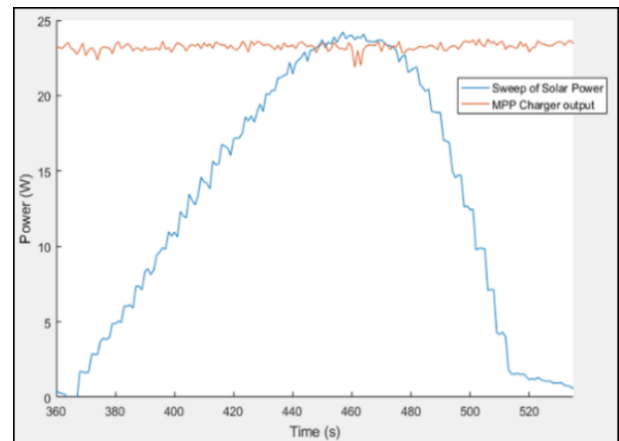


Fig. 16: Verification of MPPT Charge Controller.

The physical specifications of the completed system are given in table 3. The basic specifications of the aircraft and the completed system are given in this table. The specifications such as the wing area of the aircraft were specified as they were provided by the manufacturer of the aircraft and are somewhat difficult to accurately measure by hand.

The power output of the solar cells was recorded during a typical sunny day in October. This power output was recorded at about 1 o'clock in the afternoon. Figure 17 shows the power output of the solar panels. From about the 20 seconds to 45 seconds point on the graph, the sun light was obstructed by cloud cover which is why the power output of the solar cells dropped during that period. The solar array outputted about 35W of power under ideal conditions, although 22 solar cells were integrated into the aircraft. Each solar cell was specified by the supplier to produce about 3.3W per cell, although under practical conditions the solar cells

only produce about 1.59W per cell. The solar cells thus only produced about half their expected power output. Seeing that the battery that was used in the aircraft was obtained from a previous final year project, the battery was depleted by operating the motor at a certain power to check if the batteries capacity was still as specified. Figure 18 shows the results of the rundown test that was done on the Li-PO battery. The battery is a 4-cell LiPO battery with a rated capacity of 6000 mAh.

Table 3: Aircraft Specifications

Aircraft Specifications	
Length (m)	1.078 m
Wingspan (m)	2 m
Height (cm)	32 cm
Weight (Excluding Monitoring System) (kg)	2.842 kg
Weight (Including Monitoring System) (kg)	2.896 kg
Communication range (m)	0 – 950 m

The battery was only operated until a low-cell voltage alarm was activated. This alarm is activated when one of the cells in the battery reaches a voltage of 3.6 V. Note from this graph that the yellow line, representing the motor being operated at 5 A, that the battery only lasted for about 2600 seconds or 43.3 minutes. The battery thus had a usable battery capacity of about 3600 mAh. Using the data that was collected from running the motor at 10 A and noting that the motor operated for 1800 seconds or 30 minutes, the practical battery capacity in this case was about 5000 mAh. Using the data that was collected from running the motor at 15 A, we note that the practical battery capacity was about 1667 mAh.

The practical battery capacity thus varied quite a lot, depending on the load on the battery. This could also be due to the fact that the one cell of the battery was somewhat damaged. During testing it was found that the one cell of the battery would always trigger the low-voltage alarm. This cell's voltage was about 0.2 V below that of the other three cells, even though the battery's cells' voltages were balanced at full charge. Due to the fact that the battery was somewhat compromised, it was decided that the aircraft would not be operated until the battery was depleted. The maximum flight range of the aircraft was thus not tested, but the power consumption of the aircraft was monitored during test flights. The power consumption of the aircraft was monitored during this test flight and is shown in figure 19.

During the take-off and climbing portion of the test flight, we note that the power consumption of the aircraft is high, using about 325 W during this period. After the aircraft reached altitude, the aircraft was flown in a circuit, constantly turning to stay within range of the transmitter. The aircraft loses some altitude while turning. The fact that the aircraft was turning and losing altitude meant that the aircraft consumed more power during this period than the aircraft would have if it was flying at a constant speed. This explains the spikes in the power consumption of the aircraft during the mixed flying period. On average the aircraft used between a 100 W to 175 W at cruise speed. During the landing phase the power consumption of the aircraft is low as we would expect, seeing that the motor was then only used to ensure that the aircraft had enough airspeed not to stall.

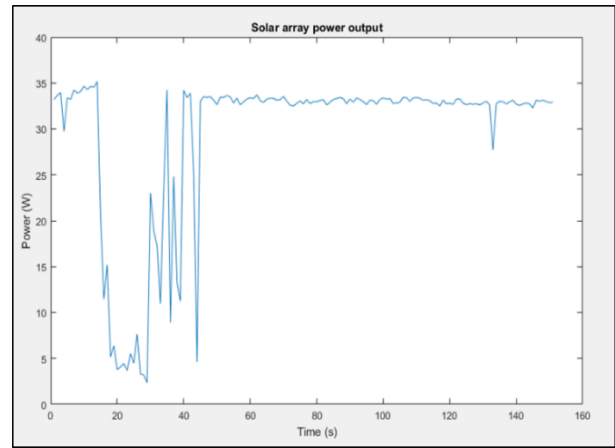


Fig. 17: Power Output of Solar Array.

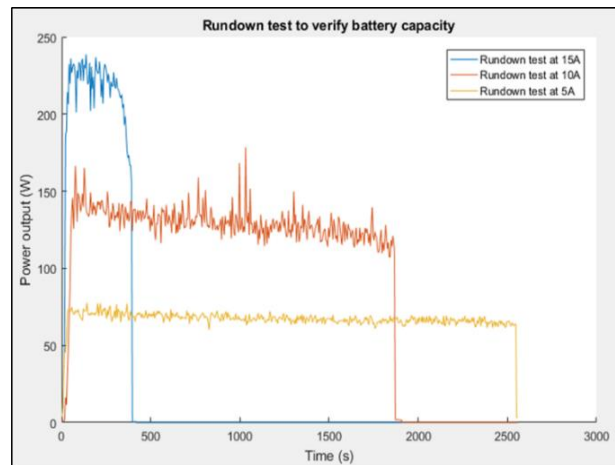


Fig. 18: Battery Rundown Test.

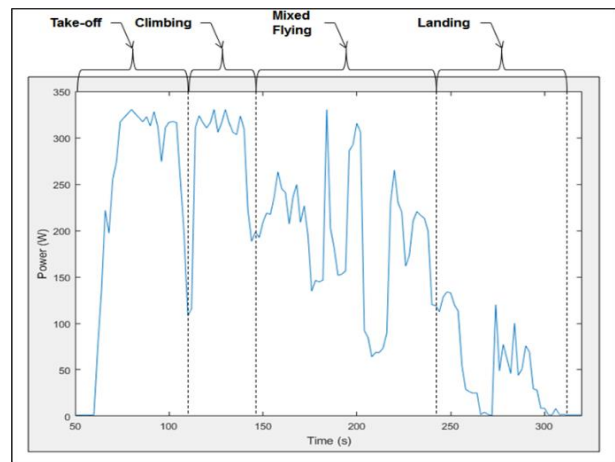


Fig. 19: Power Consumption of Aircraft during Test Flight.

The solar array on the aircraft produced about 35 W of power under ideal conditions. If the aircraft was to be operated at a time during the day in which the sun's irradiation levels were sufficient, the solar cells would supply 20 % to 35 % of the energy consumed by the aircraft. If it is assumed that the take-off and landing period only accounts for 10% of the total flight time of the aircraft, the solar cells would provide between 20% to 35% of the aircrafts energy needs during the middle portion of the flight in which the aircraft flies at cruise speed, which accounts for 90 % of the flight. Using this information, table 4 was created, predicting the flight duration of the aircraft with and without the use of the solar cells. The table compares the flight duration of the aircraft if batteries with different capacities were used. The flight duration is also calculated while the aircraft operates at different power consumption levels during cruise speed. The calculations were done by making the following assumptions: 1) the solar cells provide a

constant power output of 30W for the duration of the flight, 2) the batteries provide 100% of their capacity and, 3) the aircraft uses as constant amount of power for the duration of the flight.

As we note from the table, the solar cells had the greatest impact on the flight duration of the aircraft when the power consumption of the aircraft was the lowest, as we would expect. It is thus vital to reduce the overall power consumption of the aircraft. One of the methods to reduce this is by reducing the overall weight of the aircraft. The next section shows the weight distribution of the aircraft.

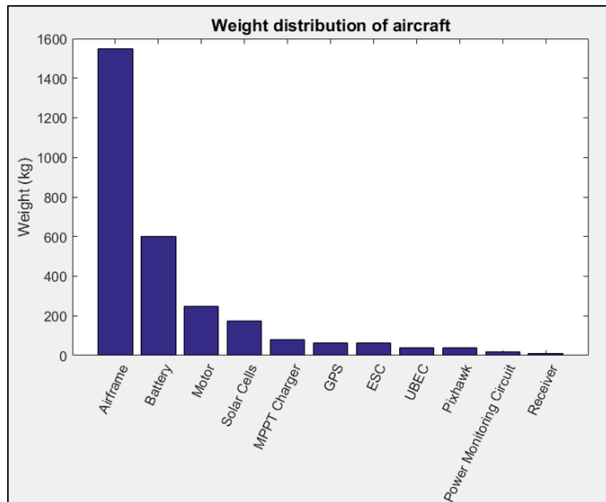


Fig. 20: Weight Distribution of the Aircrafts Components.

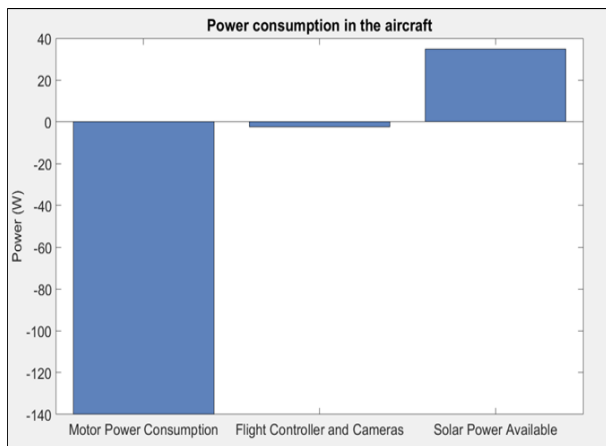


Fig. 21: Power Distribution of the Aircraft.

The overall weight distribution of the various components in the aircraft is shown in figure 20. As noted from the figure, the battery contributed 20% to the total weight of the aircraft, while the solar cells only contributed 6% to the total weight of the aircraft. The total weight of the aircraft was 2.9 kg. The airframe of the aircraft contributed 59% of the aircrafts total weight.

The power consumption of the aircraft’s motor, the monitoring system and flight controller and the energy available from the solar cell is shown in figure 21.

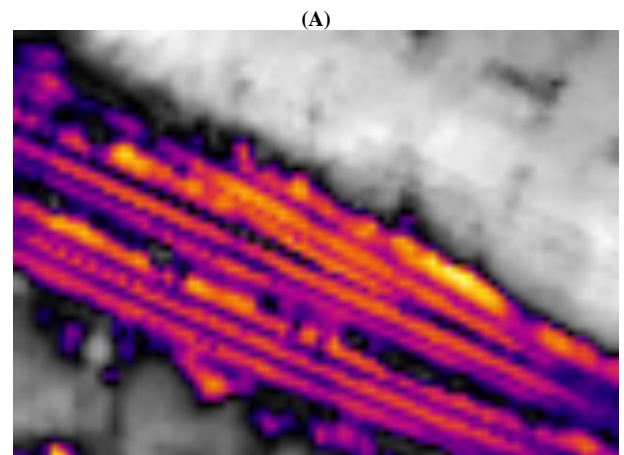
From figure 21, the power consumption of the flight controller and the cameras of the monitoring system is negligible in comparison to that of the power consumption of the aircrafts motor. Minimizing the energy used by the aircrafts motor and increasing the output power of the solar cells would drastically increase the flight range of the aircraft.

Figure 22 show examples of the images captured using the Pi and FLIR camera. After some complications in flying the plane, including poor weather conditions and the fact that a professional was required to fly the plane, the Pi and cameras were strapped to a UAV and flown over nearby train tracks. The images are of train tracks, because the tracks would have been hot from the sun and would show up as a clear colour distinction in the thermal images.

This also demonstrates another possible application for the solar powered plane, railway condition monitoring.

Table 4: Flight Time Estimation of the Aircraft

Aircraft Power Consumption		100 W	125 W	150 W	175 W
Battery Capacity: 4000 mAh	Without Solar Cells	36	29	24	20
	With Solar Cells	51	37	30	25
	Cells	min	min	min	min
Battery Capacity: 6000 mAh	Without Solar Cells	54	43,2	36	30,1
	With Solar Cells	77	57	45	37
	Cells	min	min	min	min
Battery Capacity 10,000 mAh	Without Solar Cells	90	72	60	51
	With Solar Cells	128	94	75	62
	Cells	min	min	min	min



(A)



(B)

Fig. 25: Examples Of Images Captured.

From the images it is clear that the Pi camera’s resolution is not high enough to capture a lot of detail. Its lack of physical shutter is problematic, because there was minor warping of the image caused by the vibration of the UAV. This would have been solved by using a camera with a hardware shutter and being able to configure the shutter speed. The FLIR camera exceeded expectations, seeing as it has an inherently low resolution of 80x60 pixels. In the images there are clear temperature distinctions between the warm tracks and the cold spaces between them, instead of it being a big hot spot due to the low resolution. A higher resolution FLIR camera would have still been better and preferred, but the budget did not allow for this.

Testing the GPS was also simultaneously a test of the Pi-to-Pixhawk MAVLink communication. Using the dronekit python module, and the wrapper class written, the flight controller was

queried for its current location. The function "getContext()" retrieves the planes GPS position, including altitude, as well as its current groundspeed.

It was observed that the received coordinates are just over 20 m away from the actual position. This inaccuracy may be attributed to the fact that the test was done indoors and the GPS didn't have a very accurate lock. Nevertheless, in the case of the plane flying over a single row of transmission lines, this radius of accuracy isn't ideal, but remains usable.

The "weather.com" web API through the pywapi Python module was used to give minimum and maximum temperatures in degrees Celsius, relative humidity in percentage, wind gusts in km/h, chance of rain in percentage and average wind speed in km/h. It was decided that wind speeds of more than 20 km/h or a more than 50% chance of rain is considered unsafe flying weather, so the Pi would disarm the flight controller and log a message noting the unsafe conditions.

4. Conclusion

Overall the project was successful in integrating the solar cells into an aircraft to increase the flight range of the aircraft. The designed circuits worked correctly and worked as intended, monitoring the power consumption of the aircraft and successfully charging the batteries of the aircraft by using these solar cells. The addition of the solar cells was beneficial to the overall flight performance of the aircraft, only contributing 6% to the aircrafts total weight, while theoretically supply 20% to 35% of the aircrafts energy needs. This would result in an approximate increase in the flight range of the aircraft of about 20%.

In the results, all individual hardware and software components functioned as expected. The system as a whole, attached to the plane and relying solely on the flight controller's auto-pilot, could not be tested because of complications and time constraints. The cameras were strapped to a UAV to be able to capture images for review and testing purposes. The colour images were of high enough quality, but some warping and blurring occurred as a result of the UAV's vibration and the camera's lack of a hardware shutter. The FLIR camera performed excellently, despite its low resolution and clear temperature and object distinctions could be made. The GPS showed an accuracy of around 20 m, possibly due to the surrounding buildings, where the test was conducted, interfering with the signal. The GUI was functional and succeeded in being user-friendly and intuitive. The user was able to sign in, choose which day's data and images to view and scroll through the different images, viewing their GPS coordinates, the plane's altitude and ground speed.

References

- [1] Eskom, "Company information overview," Eskom, [Online]. Available: http://www.eskom.co.za/OurCompany/CompanyInformation/Pages/Company_Information.aspx. [Accessed 15 February 2017].
- [2] Eskom, "Integrated report 2016," Eskom, 31 March 2016. [Online]. Available: http://www.eskom.co.za/IR2016/Documents/Eskom_integrated_report_2016.pdf. [Accessed 15 February 2017].
- [3] S. Lau, "A plan for reducing wire strike incidents," in Professional Pilot, Alexandria, Queensmith Communications Corp, 2012, p. 87.
- [4] S. Wan, X. Bian, L. Chen and L. Wang, "Safety Distance Determination for 500 kV AC Transmission Line's Helicopter Inspection," Scientific Research Publishing, vol. 5, no. 4B, pp. 1, 1154, 2013.
- [5] A. Pagnano, M. Hopf and R. Teti, "A roadmap for Automated Power Line Inspection, Maintenance and Repair," in CIRP Conference on Intelligent Computation in Manufacturing Engineering, 2013. <https://doi.org/10.1016/j.procir.2013.09.041>.
- [6] J. Katrasnik, F. Pernus and B. Likar, "A Survey of Mobile Robots for Distribution Power Line Inspection," IEEE Transactions on Power Delivery, vol. 25, no. 1, pp. 485 - 493, 2010. <https://doi.org/10.1109/TPWRD.2009.2035427>.

- [7] L. F. Luque-Vega and B. Castillo-Toledo, "Power line inspection via an unmanned aerial system based on the quadrotor helicopter," in Mediterranean Electrotechnical Conference, 17th IEEE, 2014.
- [8] B. Wang, X. Chen and L. Liu, "Power line inspection with a flying robot," in 1st International Conference on Applied Robotics for the Power Industry, 2010. <https://doi.org/10.1109/CARPI.2010.5624430>.
- [9] S. Bouchard, "LineScout Robot Climbs on Live Power Lines to Inspect Them," IEEE Spectrum, 13 Augustus 2010. [Online]. Available: <http://spectrum.ieee.org/automaton/robotics/industrial-robots/linescout-robot-climbs-on-live-power-lines-to-inspect-them>. [Accessed 16 February 2017].
- [10] A.-M. Corley, "Robotic Tightrope Walkers for High-Voltage Lines," IEEE Spectrum, 12 November 2009. [Online]. Available: <http://spectrum.ieee.org/robotics/industrial-robots/robotic-tightrope-walkers-for-highvoltage-lines/0>. [Accessed 16 February 2017].
- [11] W. C. UAV, "Major Milestone: Comms Network Controls Multiple UAVs," West Coast UAV, [Online]. Available: <https://westcoastuav.org/2015/09/15/major-milestone-comms-network-controls-multiple-uavs/>. [Accessed 29 April 2017].
- [12] N. Mohan, "Switch-Mode DC-DC Converters: Switching Analysis, Topology, Selection and Design," in First Course Power Electronics and Drives, Minnesota, MNPERE, 2003, pp. 3-1; 3-13.
- [13] I. Glasner and J. Appelbaum, "Advantage of boost vs. buck topology for maximum power point tracker in photovoltaic systems," Proceedings of 19th Convention of Electrical and Electronics Engineers in Israel, pp. 355-358, 1996. <https://doi.org/10.1109/EEIS.1996.566988>.
- [14] J. Mirek, "Propeller Efficiency," RCEX, 26 November 2010. [Online]. Available: <http://www.rcex.cz/?p=3593>. [Accessed 4 April 2017].